Small-Signal Stability Analysis of an Inverter-Based Microgrid with Internal Model–Based Controllers

Stefan Leitner, *Graduate Student Member, IEEE*, Mehrdad Yazdanian, *Graduate Student Member, IEEE*,
Ali Mehrizi-Sani, *Senior Member, IEEE*, and Annette Muetze, *Fellow, IEEE*

***Abstract*—Several microgrid control strategies are proposed and studied in the literature. However, there are still gaps in improving their transient behavior and studying their stability. This paper uses small-signal analysis to explore the behavior of internal model–based current and voltage controllers by deriving a state-space model and performing eigenvalue and sensitivity analysis on an islanded inverter-based microgrid system. The results are compared with those of the same microgrid but with PI-based current and voltage controllers. Simulation case studies are performed in the PSCAD/EMTDC environment to compare the transient behavior of both methods. Results show that internal model–based controllers have superior eigenvalue patterns that lead to increased stability and improved transient behavior.**

***Index Terms*—Current control, eigenvalues, internal model control, islanded microgrid, inverter, small-signal stability, state-space model, voltage control, voltage-sourced converter.**

I. INTRODUCTION

In recent years, electricity generation from distributed energy resources, e.g., photovoltaics, microturbines, and fuel cells, has increased significantly. Control and management of small-scale distributed generator (DG) units pose a significant challenge compared to the existing practices for large centralized generating stations [1]–[6]. Microgrids can help integrate DG units effectively and in turn improve the reliability and sustainability of the power grid [7]. A microgrid can operate in both grid-connected and islanded operating modes [8]–[10]. In the grid-connected mode, the voltage and frequency are dictated by the main grid. However, in the islanded mode, the controllers of the DG units in the microgrid are responsible for regulation of voltage and frequency and for power sharing between DG units [11]–[14].

Many DG units utilize power electronic inverters, especially voltage-sourced converters (VSC), to interface with the microgrid [15], [16]. The key advantages of a power electronics–based interface are improved power quality, voltage regulation, fault current coordination, and reactive power (VAr) support [17]. On the downside, inverter-based microgrids have low inertia, which causes challenges in maintaining stability and mitigating oscillations.

The various approaches that have been proposed for current or voltage regulation of three-phase VSCs can be categorized into two main groups: nonlinear and linear approaches. Nonlinear approaches increase the complexity of the system in terms of design and implementation, while they do not necessarily provide superior performance compared with linear methods [18]. Linear methods in turn can be classified into two main groups: stationary reference frame (SRF)-based and rotating reference frame (RRF)-based approaches. Often, SRF-based approaches suffer from a considerable steady-state error [19], while RRF-based approaches can provide zero steady-state error. Among RRF-based approaches, PI-based current and voltage regulators are the most widely used. PI-based controllers are extensively studied in the literature [11], [12], [20]–[23] and dominate the zero-level control in inverter-based microgrids [12]. PI control, although effective, widely used, and easy to tune, has a slow response, a large overshoot, and a long settling time. It also lacks robustness and axes decoupling. Improving stability and transient behavior of voltage and current is imperative for microgrids to allow more effective utilization of the assets and prevent violation of the operational limits [24], [25].

Recently, [26], [27] proposed a cascade internal model control (IMC)–based voltage regulator consisting of an inner current and an outer voltage controller, as shown in Fig. 1. The authors perform time-domain simulations for a single DG unit and show that compared with PI-based controllers, the IMC-based approach has superior transient performance and is more robust against system parameter uncertainties. However, these studies are limited to a single DG unit and no systematic stability analysis is performed. In fact, while small-signal models are widely used in the literature, especially for PI-based controllers [11], [28], small-signal models for IMC-based controllers have not been developed yet.

This paper studies the small-signal stability and transient behavior of a microgrid with IMC-based current and voltage controllers and provides an insight into the superior transient behavior of IMC controllers. As the first step, the state-space models of the current and voltage controllers are developed. Then, the state-space model of a microgrid with IMC-based controllers is developed following the procedure in [11]. Using this model, a detailed small-signal stability analysis is performed for a study microgrid system with three DG units and the results are compared with those of the same microgrid but with cascade PI-based controllers utilized in [11]. Moreover, PSCAD simulation studies on transient behavior of the microgrid are performed for both methods to confirm the results of the small-signal analysis.

This study shows that, compared with PI-based controllers, IMC-based controllers have

- Increased damping ratios of sensitive eigenvalues;
- Higher robustness to parameter changes; and
- Faster step response and reduced over/undershoot in current and voltage transients.

This work is supported in part by the Austrian Marshall Plan Foundation through scholarship number 639 848 22 15 2015 and in part by the National Science Foundation award number ECCS-1509895.

S. Leitner and A. Muetze are with the Electrical Drives and Machines Institute at Graz University of Technology, Graz, Austria, 8010 (e-mails: s.leitner@tugraz.at, muetze@tugraz.at).

M. Yazdanian and A. Mehrizi-Sani are with the Energy Systems Innovation (ESI) Center and the School of Electrical Engineering and Computer Science, Washington State University, Pullman, WA, USA, 99164-2752 (e-mails: m.yazdanian@email.wsu.edu, mehrizi@eecs.wsu.edu).

This article has been accepted for publication in a future issue of this journal, but has not been fully edited. Content may change prior to final publication. Citation information: DOI 10.1109/TSG.2017.2688481, IEEE Transactions on Smart Grid

These advantages agree with the transient behavior of a single DG unit obtained from time-domain simulation in [27].

The rest of this paper is organized as follows. Section II derives the state-space models for the IMC-based current and voltage controllers. The model of the complete microgrid is presented in Section III. Sections IV and V discuss the results of the small-signal analysis and simulation studies. Finally, Section VI recapitulates the study and draws conclusions.

II. STATE-SPACE MODEL OF IMC-BASED VOLTAGE AND CURRENT CONTROLLERS

This section derives the small-signal state-space model for the IMC-based voltage and current controllers illustrated in Fig. 1. Generally, the integrator outputs are selected as the state variables, which in turn makes their inputs derivatives of the state. Hence, the state equations for the inner current control loop, in direct and quadrature axes, are

$$\frac{d\gamma_d}{dt} = i^*_{ld} - i_{ld} \qquad \text{and} \qquad \frac{d\gamma_q}{dt} = i^*_{lq} - i_{lq}, \tag{1}$$

and those of the outer voltage control loop are

$$\frac{d\phi_d}{dt} = v^*_{od} - v_{od} \qquad \text{and} \qquad \frac{d\phi_q}{dt} = v^*_{oq} - v_{oq}, \tag{2}$$

where γ_d, γ_q, ϕ_d, and ϕ_q are the state variables. For notational brevity, time functions are stated without (t). The definition of all voltages and currents are based on Fig. 2. Subscripts d and q represent direct and quadrature axes, respectively, and $*$ refers to the reference value of a variable. Throughout the paper, d- and q-components of the input vectors, output vectors, and state variables of the state-space small-signal models are aggregated as $z_{dq} = [z_d \ z_q]^T$.

A. Current Controller

This subsection derives the small-signal model of the inner current control loop shown in Fig. 1. In [27], transfer functions $K_c(s)$ and $K'_c(s)$ are PID and PI controllers, respectively, with the tuning parameters K_{Pc}, K_{Ic}, K_{Dc}, K'_{Pc}, and K'_{Ic}. However, since a state-space representation requires proper transfer functions, the derivative terms of controllers are neglected, which is justifiable in this study as K_{Pc} and K_{Ic} are four and six orders of magnitude greater than K_{Dc} [27]. From Fig. 1, the output equations of the inner current control loop are

$$\begin{aligned} v_{id}(s) = v_{od}(s) &+ \underbrace{\left[K_{Pc} + \frac{K_{Ic}}{s}\right]}_{K_c(s)} \left[i^*_{ld}(s) - i_{ld}(s)\right] \\ &- \underbrace{\left[K'_{Pc} + \frac{K'_{Ic}}{s}\right]}_{K'_c(s)} \left[i^*_{lq}(s) - i_{lq}(s)\right] \end{aligned} \tag{3}$$

$$\begin{aligned} v_{iq}(s) = v_{oq}(s) &+ \underbrace{\left[K_{Pc} + \frac{K_{Ic}}{s}\right]}_{K_c(s)} \left[i^*_{lq}(s) - i_{lq}(s)\right] \\ &+ \underbrace{\left[K'_{Pc} + \frac{K'_{Ic}}{s}\right]}_{K'_c(s)} \left[i^*_{ld}(s) - i_{ld}(s)\right]. \end{aligned} \tag{4}$$

Applying inverse Laplace transform to (3) and (4) and taking (1) into account yields

$$\begin{aligned} v_{id} = v_{od} &+ K_{Pc} i^*_{ld} - K_{Pc} i_{ld} + K_{Ic}\gamma_d \\ &- K'_{Pc} i^*_{iq} + K'_{Pc} i_{lq} - K'_{Ic}\gamma_q \end{aligned} \tag{5}$$

$$\begin{aligned} v_{iq} = v_{oq} &+ K_{Pc} i^*_{lq} - K_{Pc} i_{lq} + K_{Ic}\gamma_q \\ &+ K'_{Pc} i^*_{ld} - K'_{Pc} i_{ld} + K'_{Ic}\gamma_q. \end{aligned} \tag{6}$$

By linearizing and combining (1), (5), and (6), the small-signal state-space model of the inner current control loop is obtained as

$$\begin{aligned} \left[\Delta\dot{\gamma}_{dq}\right] = & \underbrace{\begin{bmatrix} 0 & 0 \\ 0 & 0 \end{bmatrix}}_{A_I} \left[\Delta\gamma_{dq}\right] + \underbrace{\begin{bmatrix} 1 & 0 \\ 0 & 1 \end{bmatrix}}_{B_{I1}} \left[\Delta i^*_{ldq}\right] \\ & + \underbrace{\begin{bmatrix} -1 & 0 & 0 & 0 & 0 & 0 \\ 0 & -1 & 0 & 0 & 0 & 0 \end{bmatrix}}_{B_{I2}} \begin{bmatrix} \Delta i_{ldq} \\ \Delta v_{odq} \\ \Delta i_{odq} \end{bmatrix} \end{aligned} \tag{7}$$

$$\begin{aligned} \left[\Delta v_{idq}\right] = & \underbrace{\begin{bmatrix} K_{Ic} & -K'_{Ic} \\ K'_{Ic} & K_{Ic} \end{bmatrix}}_{C_I} \left[\Delta\gamma_{dq}\right] + \underbrace{\begin{bmatrix} K_{Pc} & -K'_{Pc} \\ K'_{Pc} & K_{Pc} \end{bmatrix}}_{D_{I1}} \left[\Delta i^*_{ldq}\right] \\ & + \underbrace{\begin{bmatrix} -K_{Pc} & K'_{Pc} & 1 & 0 & 0 & 0 \\ -K'_{Pc} & -K_{Pc} & 0 & 1 & 0 & 0 \end{bmatrix}}_{D_{I2}} \begin{bmatrix} \Delta i_{ldq} \\ \Delta v_{odq} \\ \Delta i_{odq} \end{bmatrix}. \end{aligned} \tag{8}$$

B. Voltage Controller

This subsection derives the small-signal model of the outer voltage control loop depicted in Fig. 1. In [27], the transfer functions $K_v(s)$ and $K'_v(s)$ are PD and PI controllers, respectively, with the tuning parameters K_{Pv}, K_{Dv}, K'_{Pv}, and K'_{Iv}. Again, the derivative terms are omitted since a state-space representation needs proper transfer functions, which is justifiable in this study because K_{Dv} is 500 times smaller than K_{Pv}. The output equations of the outer voltage control loop can be derived from Fig. 1 as follows:

$$\begin{aligned} i^*_{ld}(s) = i_{od}(s) &+ \underbrace{K_{Pv}}_{K_v(s)} \left[v^*_{od}(s) - v_{od}(s)\right] \\ &- \underbrace{\left[K'_{Pv} + \frac{K'_{Iv}}{s}\right]}_{K'_v(s)} \left[v^*_{oq}(s) - v_{oq}(s)\right] \end{aligned} \tag{9}$$

$$\begin{aligned} i^*_{lq}(s) = i_{oq}(s) &+ \underbrace{K_{Pv}}_{K_v(s)} \left[v^*_{oq}(s) - v_{oq}(s)\right] \\ &+ \underbrace{\left[K'_{Pv} + \frac{K'_{Iv}}{s}\right]}_{K'_v(s)} \left[v^*_{od}(s) - v_{od}(s)\right]. \end{aligned} \tag{10}$$

Applying inverse Laplace transform to (9) and (10), and taking (2) into account, the following algebraic equations for the outer voltage control loop can be derived:

$$\begin{aligned} i^*_{ld} = i_{od} &+ K_{Pv} v^*_{od} - K_{Pv} v_{od} \\ &- K'_{Pv} v^*_{oq} + K'_{Pv} v_{oq} - K'_{Iv}\phi_q \end{aligned} \tag{11}$$

This article has been accepted for publication in a future issue of this journal, but has not been fully edited. Content may change prior to final publication. Citation information: DOI 10.1109/TSG.2017.2688481, IEEE Transactions on Smart Grid

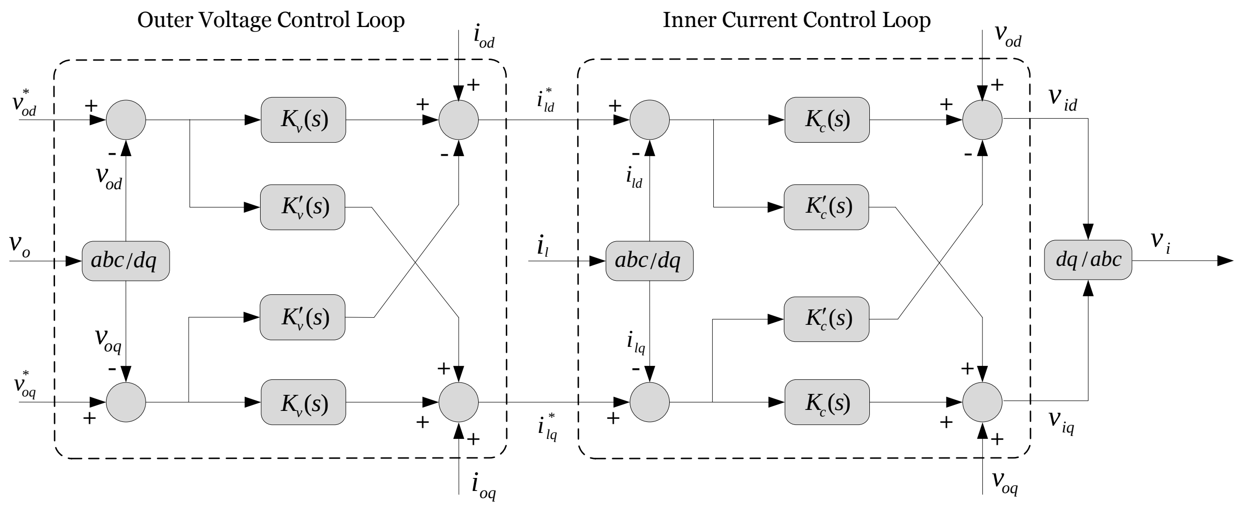

Fig. 1. Block diagram of the IMC-based cascade voltage and current controllers of a VSC in the rotating dq reference frame [27].

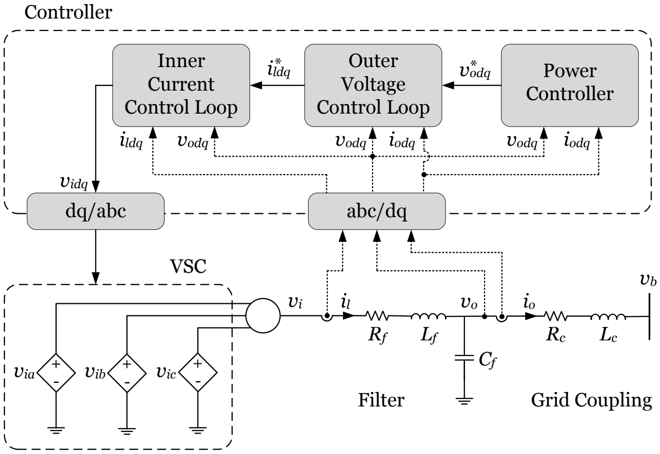

Fig. 2. DG unit block diagram including controllers, VSC, filter, and grid coupling.

$$\begin{aligned} i_{lq}^* = i_{oq} + K_{Pv}v_{oq}^* - K_{Pv}v_{oq} \\ + K_{Pv}'v_{od}^* - K_{Pv}'v_{od} + K_{Iv}'\phi_d. \end{aligned} \tag{12}$$

By linearizing and combining (2), (11), and (12), the small-signal model of the outer voltage control loop in state-space form can be written as follows:

$$\begin{aligned} [\Delta\dot{\phi}_{dq}] &= \underbrace{\begin{bmatrix} 0 & 0 \\ 0 & 0 \end{bmatrix}}_{A_V} [\Delta\phi_{dq}] + \underbrace{\begin{bmatrix} 1 & 0 \\ 0 & 1 \end{bmatrix}}_{B_{V1}} [\Delta v_{odq}^*] \\ &+ \underbrace{\begin{bmatrix} 0 & 0 & -1 & 0 & 0 & 0 \\ 0 & 0 & 0 & -1 & 0 & 0 \end{bmatrix}}_{B_{V2}} \begin{bmatrix} \Delta i_{ldq} \\ \Delta v_{odq} \\ \Delta i_{odq} \end{bmatrix} \end{aligned} \tag{13}$$

$$\begin{aligned} [\Delta i_{ldq}^*] &= \underbrace{\begin{bmatrix} 0 & -K_{Iv}' \\ K_{Iv}' & 0 \end{bmatrix}}_{C_V} [\Delta\phi_{dq}] + \underbrace{\begin{bmatrix} K_{Pv} & -K_{Pv}' \\ K_{Pv}' & K_{Pv} \end{bmatrix}}_{D_{V1}} [\Delta v_{odq}^*] \\ &+ \underbrace{\begin{bmatrix} 0 & 0 & -K_{Pv} & K_{Pv}' & 1 & 0 \\ 0 & 0 & -K_{Pv}' & -K_{Pv} & 0 & 1 \end{bmatrix}}_{D_{V2}} \begin{bmatrix} \Delta i_{ldq} \\ \Delta v_{odq} \\ \Delta i_{odq} \end{bmatrix}. \end{aligned} \tag{14}$$

The design procedure for the control parameters K_{Pv}, K_{Pv}', K_{Iv}', K_{Pc}, K_{Ic}, K_{Pc}', and K_{Ic}' is presented in [27]. The inverter is modeled as a time delay $T_{\text{PWM}} = 1/(2f_{\text{sw}}) = 1/(2 \times 8000 \text{ Hz}) = 6.25 \times 10^{-5}$ s. The IMC tuning parameters λ_c and λ_v represent the closed-loop time constants of the current and voltage control loops. Their values are first estimated and then fine-tuned with a MATLAB/Simulink model of a VSC by successively varying the parameters. Finally, with $\lambda_c = 10^{-5}$ and $\lambda_v = 2 \times 10^{-4}$, the control parameters of the current and voltage controllers are chosen as

$$\begin{cases} K_{Pc} = \frac{R_f T_{\text{PWM}} + L_f}{\lambda_c} = \frac{0.1\ \Omega \times 6.25 \times 10^{-5}\ \text{s} + 1.35\ \text{mH}}{10^{-5}} = 135.625 \\ K_{Ic} = \frac{R_f + T_{\text{PWM}} L_f \omega^2}{\lambda_c} = \frac{0.1\ \Omega + 6.25 \times 10^{-5}\ \text{s} \times 1.35\ \text{mH} \times (2\pi 50\ \text{Hz})^2}{10^{-5}} \\ \quad = 9.1673 \times 10^3 \\ K_{Dc} = \frac{T_{\text{PWM}} L_f}{\lambda_c} = \frac{6.25 \times 10^{-5}\ \text{s} \times 1.35\ \text{mH}}{10^{-5}} = 0.0084 \end{cases} \tag{15}$$

$$\begin{cases} K_{Pc}' = \frac{2\omega L_f T_{\text{PWM}}}{\lambda_c} = \frac{2 \times 2\pi 50\ \text{Hz} \times 1.35\ \text{mH} \times 6.25 \times 10^{-5}\ \text{s}}{10^{-5}} \\ \quad = 5.3014 \\ K_{Ic}' = \frac{2(L_f + R_f T_{\text{PWM}})}{\lambda_c} = \frac{2(1.35\ \text{mH} + 0.1\ \Omega \times 6.25 \times 10^{-5}\ \text{s})}{10^{-5}} \\ \quad = 4.2608 \times 10^4 \end{cases} \tag{16}$$

$$\begin{cases} K_{Pv} = \frac{C_f}{\lambda_v} = \frac{50\ \mu\text{F}}{2 \times 10^{-4}} = 0.25 \\ K_{Dv} = \frac{C_f T_c}{\lambda_v} = \frac{50\ \mu F \times 2\ \text{ms}}{2 \times 10^{-4}} = 5 \times 10^{-4} \end{cases} \tag{17}$$

$$\begin{cases} K_{Pv}' = \frac{C_f \omega T_c}{\lambda_v} = \frac{50\ \mu F \times 2\pi 50\ \text{Hz} \times 2\ \text{ms}}{2 \times 10^{-4}} = 0.1571 \\ K_{Iv}' = \frac{2 C_f \omega}{\lambda_v} = \frac{2 \times 50\ \mu\text{F} \times 2\pi 50\ \text{Hz}}{2 \times 10^{-4}} = 78.5398. \end{cases} \tag{18}$$

The control parameters used in this paper for the conventional method are the same as those reported in [11].

III. STATE-SPACE MODEL OF A GENERIC MICROGRID

This section discusses the small-signal model of a microgrid study system that includes power controllers, filters, inverters, lines, and loads [11]. It is shown how the submodels combine to form the linearized system matrix A_{MG}. The notation `diag()` is used to show the nonzero elements of a diagonal matrix.

A. Power Controller Model

While there are elaborate droop control methods (e.g., [29]), for comparison, this study utilizes a conventional droop control–based power controller to share real and reactive power between microgrid inverters as shown in Fig. 3. The dq-components of the DG unit output current and voltage (see Fig. 2)are used to calculate the instantaneous real and reactive power components $\tilde{p}$ and $\tilde{q}$. These signals are low-pass filtered with a cut-off frequency of ω_c. The resulting average values P and Q are used in the droop equation (see Fig. 3). With the droop control, an increase in the real output power artificially reduces the reference value of the inverter frequency ω^*. Similarly, an increase in the reactive output power reduces the reference output voltage v^*_{od} of the inverter while v^*_{oq} is set to zero. The small-signal state-space model of the droop control–based power controller is

$$\begin{bmatrix}\dot{\Delta\delta}\\ \dot{\Delta P}\\ \dot{\Delta Q}\end{bmatrix} = \underbrace{\begin{bmatrix}0 & -m_p & 0\\ 0 & -\omega_c & 0\\ 0 & 0 & -\omega_c\end{bmatrix}}_{A_P}\begin{bmatrix}\Delta\delta\\ \Delta P\\ \Delta Q\end{bmatrix} + \underbrace{\begin{bmatrix}-1\\ 0\\ 0\end{bmatrix}}_{B_{P\omega\text{com}}}\Delta\omega_{\text{com}}$$
$$+\underbrace{\begin{bmatrix}0 & 0 & 0 & 0 & 0 & 0\\ 0 & 0 & \omega_c I_{od} & \omega_c I_{oq} & \omega_c V_{od} & \omega_c V_{oq}\\ 0 & 0 & -\omega_c I_{oq} & \omega_c I_{od} & \omega_c V_{oq} & -\omega_c V_{od}\end{bmatrix}}_{B_P}\begin{bmatrix}\Delta i_{ldq}\\ \Delta v_{odq}\\ \Delta i_{odq}\end{bmatrix} \tag{19}$$

$$\begin{bmatrix}\Delta\omega^*\\ \Delta v^*_{od}\\ \Delta v^*_{oq}\end{bmatrix} = \underbrace{\begin{bmatrix}0 & -m_p & 0\\ 0 & 0 & -n_q\\ 0 & 0 & 0\end{bmatrix}}_{C_P}\begin{bmatrix}\Delta\delta\\ \Delta P\\ \Delta Q\end{bmatrix}, \tag{20}$$

where the angle δ_i describes the displacement of inverter i quantities from the reference inverter rotating at ω_{com}. The coefficients m_p and n_q are the real and reactive power droop gains, which depend on the DG unit ratings (P_{max}, Q_{min}, Q_{max}) and the grid code (f_{max}, f_{min}, V_{max}, V_{min}). Quantities I_{od}, I_{oq}, V_{od}, and V_{oq} are the steady state values representing the operating point for linearization takes place. For comparison, m_p, n_q, I_{od}, I_{oq}, V_{od}, and V_{oq} are taken from [11].

B. Small-Signal Model Matrices of Filters, Lines, Loads, and Variable Transformations

The submatrices discussed in this subsection are available in [11] and therefore not repeated in this paper. Matrices A_{LCL}, B_{LCL1}, B_{LCL2}, and B_{LCL3} build the small-signal model of the filter and grid coupling used in each DG unit (Fig. 2). T_{Si},

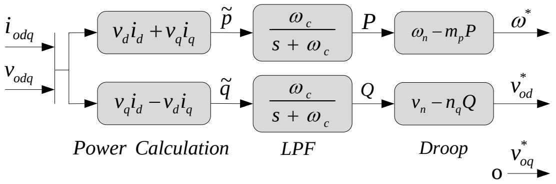

Fig. 3. Power controller.

$$A_{\text{INV}i} = \left[\begin{array}{c:c:c:c} A_{Pi} & [\mathbf{0}]_{3\times 2} & [\mathbf{0}]_{3\times 2} & B_{Pi}\\ \hdashline B_{V1i}C_{Pvi} & [\mathbf{0}]_{2\times 2} & [\mathbf{0}]_{2\times 2} & B_{V2i}\\ \hdashline B_{V1i}D_{V1i}C_{Pvi} & B_{C1i}C_{Vi} & [\mathbf{0}]_{2\times 2} & B_{C1i}D_{V2i}+B_{C2i}\\ \hdashline \begin{array}{c}B_{\text{LCL1i}}D_{C1i}D_{V1i}C_{Pvi}\\ +B_{\text{LCL2}i}\left[T_{Vi}^{-1} \,\vdots\, [\mathbf{0}]_{2\times 2}\right]\\ +B_{\text{LCL3}i}C_{P\omega i}\end{array} & B_{\text{LCL1}i}D_{C1i}C_{Vi} & B_{\text{LCL1}i}C_{Ci} & \begin{array}{c}A_{\text{LCL}i}\\ +B_{\text{LCL1}i}[D_{C1i}D_{V2i}+D_{C2i}]\end{array}\end{array}\right]_{13\times 13} \tag{19}$$

$$B_{\text{INV}i} = \left[\begin{array}{c}[\mathbf{0}]_{7\times 2}\\ \hdashline B_{\text{LCL2}i}T_{Si}^{-1}\end{array}\right]_{13\times 2} \quad B_{i\omega\text{com}} = \left[\begin{array}{c}B_{P\omega\text{com}}\\ \hdashline [\mathbf{0}]_{10\times 1}\end{array}\right]_{13\times 1} \quad C_{\text{INV}ci} = \left[\begin{array}{c:c:c}T_{Ci} & [\mathbf{0}]_{2\times 10} & T_{Si}\end{array}\right]_{2\times 13} \quad C_{Pi} = \left[\begin{array}{c}[C_{P\omega i}]_{1\times 3}\\ \hdashline [C_{Pvi}]_{2\times 3}\end{array}\right]_{3\times 3} \tag{20}$$

$$[\Delta x_{\text{INV}i}] = [\Delta\delta_i \ \Delta P_i \ \Delta Q_i \ \Delta\varphi_{dqi} \ \Delta\gamma_{dqi} \ \Delta i_{ldqi} \ \Delta v_{odqi} \ \Delta i_{odqi}]^T \qquad C_{\text{INV}\omega i} = \begin{cases}[C_{P\omega} \ 0 \ \ldots \ 0]_{1\times 13} & i = 1\\ [\mathbf{0}]_{1\times 13} & i \neq 1.\end{cases} \tag{21}$$

$$A_{\text{INV}} = \left[\begin{array}{c:c:c:c:c} A_{\text{INV1}} + B_{1\omega\text{com}}C_{\text{INV}\omega 1} & [\mathbf{0}]_{13\times 13} & [\mathbf{0}]_{13\times 13} & \cdots & [\mathbf{0}]_{13\times 13}\\ \hdashline X_{m_p} & A_{\text{INV2}} + B_{2\omega\text{com}}C_{\text{INV}\omega 2} & [\mathbf{0}]_{13\times 13} & \cdots & [\mathbf{0}]_{13\times 13}\\ \hdashline X_{m_p} & [\mathbf{0}]_{13\times 13} & \ddots & \ddots & \vdots\\ \hdashline \vdots & \vdots & \ddots & \ddots & [\mathbf{0}]_{13\times 13}\\ \hdashline X_{m_p} & [\mathbf{0}]_{13\times 13} & \cdots & [\mathbf{0}]_{13\times 13} & A_{\text{INV}k} + B_{k\omega\text{com}}C_{\text{INV}\omega k}\end{array}\right]_{13k\times 13k} \tag{24}$$

$$B_{\text{INV}} = \texttt{diag}([B_{\text{INV1}}, B_{\text{INV2}}, \ldots, B_{\text{INV}k}])_{13k\times 2m} \qquad C_{\text{INV}c} = \texttt{diag}([C_{\text{INV}c1}, C_{\text{INV}c2}, \ldots, C_{\text{INV}ck}])_{2k\times 13k} \tag{25}$$

This article has been accepted for publication in a future issue of this journal, but has not been fully edited. Content may change prior to final publication. Citation information: DOI 10.1109/TSG.2017.2688481, IEEE Transactions on Smart Grid

T_{Ci}, and T_{Vi} are matrices that transform dq-currents and voltages, according to their initial condition displacements, into a common reference frame (DQ-frame). All these matrices are part of the inverter matrices $A_{\mathrm{INV}i}$, $B_{\mathrm{INV}i}$, and $C_{\mathrm{INV}ci}$ used in Subsection III-C. Matrices A_{NET}, $B_{1\mathrm{NET}}$, $B_{2\mathrm{NET}}$, A_{LOAD}, $B_{1\mathrm{LOAD}}$, and $B_{2\mathrm{LOAD}}$ represent the small-signal models of the microgrid lines and loads. R_N, M_{INV}, M_{LOAD}, and M_{NET} build the small-signal model of the node voltages in the microgrid and ensure, by introducing large virtual resistors ($r_N = 1000\ \Omega$), that all voltages are well defined. These matrices are part of the system matrix A_{MG}, as shown in Subsection III-D.

C. Complete Model of Inverter i

In this subsection, the small-signal models of the filter and the current, voltage, and power controllers combine to form the complete model of inverter i:

$$[\Delta \dot{x}_{\mathrm{INV}i}] = A_{\mathrm{INV}i}[\Delta x_{\mathrm{INV}i}] + B_{\mathrm{INV}i}[\Delta v_{bDQi}] + B_{i\omega\mathrm{com}}\Delta\omega_{\mathrm{com}} \tag{21}$$

$$\begin{bmatrix}\Delta\omega_i \\ \Delta i_{oDQi}\end{bmatrix} = \begin{bmatrix}C_{\mathrm{INV}\omega i} \\ C_{\mathrm{INV}ci}\end{bmatrix}[\Delta x_{\mathrm{INV}i}], \tag{22}$$

where $A_{\mathrm{INV}i}$, $B_{\mathrm{INV}i}$, $B_{i\omega com}$, $C_{\mathrm{INV}\omega i}$, $C_{\mathrm{INV}ci}$, and $\Delta x_{\mathrm{INV}i}$ are defined in (19)–(21). The combined small-signal model of k inverters in a microgrid with m nodes is represented as

$$[\Delta \dot{x}_{\mathrm{INV}}] = A_{\mathrm{INV}}[\Delta x_{\mathrm{INV}}] + B_{\mathrm{INV}}[\Delta v_{bDQ}] \tag{22}$$

$$[\Delta \dot{i}_{oDQ}] = C_{\mathrm{INV}c}[\Delta x_{\mathrm{INV}}], \tag{23}$$

where A_{INV}, B_{INV}, and $C_{\mathrm{INV}c}$ are defined in (24) and (25) and inverter 1 is chosen to be the common reference frame. Each X_{m_p} matrix in (24) is a 13×13 matrix with m_p as the only nonzero element at $(1, 2)$. This entry influences the phase angles of the remaining inverters and accounts for changes in the rotational speed of the reference inverter.

State variables, input vectors, and output vectors of LTI subsystems in this paper are aggregated as follows:

$$[\Delta Z] = [\Delta Z_1\ \Delta Z_2\ \ldots\ \Delta Z_n]^T. \tag{26}$$

This procedure is also applied to $[\Delta x_{\mathrm{INV}}]$, $[\Delta v_{bDQ}]$, $[\Delta i_{oDQ}]$, and their respective derivatives.

D. System Matrix

Finally, all subsystems are combined to form the system matrix A_{MG}, shown in (27), which is used for eigenvalue and sensitivity analysis.

$$\begin{bmatrix}\Delta \dot{x}_{\mathrm{INV}} \\ \Delta \dot{i}_{\mathrm{line}DQ} \\ \Delta \dot{i}_{\mathrm{load}DQ}\end{bmatrix} = A_{\mathrm{MG}}\begin{bmatrix}\Delta x_{\mathrm{INV}} \\ \Delta i_{\mathrm{line}DQ} \\ \Delta i_{\mathrm{load}DQ}\end{bmatrix} \tag{28}$$

TABLE I
STUDY SYSTEM PARAMETERS

Parameter	Value	Parameter	Value
f	50 Hz	λ_c	10^{-5}
L_f	1.35 mH	λ_v	2×10^{-4}
R_f	0.1 Ω	T_c	2 ms
C_f	50 μF	K_{Pc}	135.625
L_c	0.35 mH	K_{Ic}	9.1673×10^3
R_c	0.03 Ω	K'_{Pc}	5.3014
ω_c	31.41 rad/s	K'_{Ic}	4.2608×10^4
m_p	9.4×10^{-5}	K_{Pv}	0.25
n_q	1.3×10^{-3}	K'_{Pv}	0.1571
r_N	1000 Ω	K'_{Iv}	78.5398
R_{LOAD1}	25 Ω	L_{LOAD1}	10 nH
R_{LOAD3}	20 Ω	L_{LOAD3}	10 nH
R_{LINE1}	0.23 Ω	L_{LINE1}	318.31 μH
R_{LINE2}	0.35 Ω	L_{LINE2}	1.8 mH

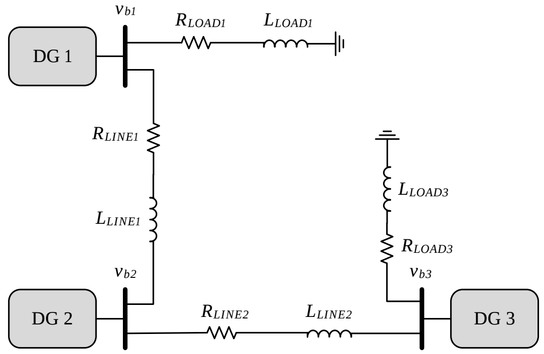

Fig. 4. Study microgrid system.

IV. SMALL-SIGNAL STABILITY AND SENSITIVITY ANALYSIS OF THE STUDY MICROGRID

In this section, the location and behavior of the eigenvalues of the study microgrid subsequent to a change in power controller parameters is investigated. Furthermore, the sensitivity of different modes to state variables is studied by calculating participation factors. Fig. 4 shows the study microgrid; it operates in the islanded mode, supplies two loads, and includes three DG units connected by two lines. Initial conditions as well as filter, line, and controller parameters are selected to be the same as in [11] to facilitate the comparison. Table I shows the parameters of the study microgrid.

A. Locus of Eigenvalues

The MATLAB function `eig()` is employed to calculate the eigenvalues of the system matrix A_{MG} and its corresponding right and left eigenvectors. Fig. 5 shows the locus of the eigenvalues of the complete model of the study microgrid using both IMC and conventional controllers. The complete system

$$A_{\mathrm{MG}} = \left[\begin{array}{c:c:c} A_{\mathrm{INV}} + B_{\mathrm{INV}}R_N M_{\mathrm{INV}}C_{\mathrm{INV}c} & B_{\mathrm{INV}}R_N M_{\mathrm{NET}} & B_{\mathrm{INV}}R_N M_{\mathrm{LOAD}} \\ \hdashline B_{1\mathrm{NET}}R_N M_{\mathrm{INV}}C_{\mathrm{INV}c} + B_{2\mathrm{NET}}C_{\mathrm{INV}\omega} & A_{\mathrm{NET}} + B_{1\mathrm{NET}}R_N M_{\mathrm{NET}} & B_{1\mathrm{NET}}R_N M_{\mathrm{LOAD}} \\ \hdashline B_{1\mathrm{LOAD}}R_N M_{\mathrm{INV}}C_{\mathrm{INV}c} + B_{2\mathrm{LOAD}}C_{\mathrm{INV}\omega} & B_{1\mathrm{LOAD}}R_N M_{\mathrm{NET}} & A_{\mathrm{LOAD}} + B_{1\mathrm{LOAD}}R_N M_{\mathrm{LOAD}} \end{array}\right] \tag{27}$$

This article has been accepted for publication in a future issue of this journal, but has not been fully edited. Content may change prior to final publication. Citation information: DOI 10.1109/TSG.2017.2688481, IEEE Transactions on Smart Grid

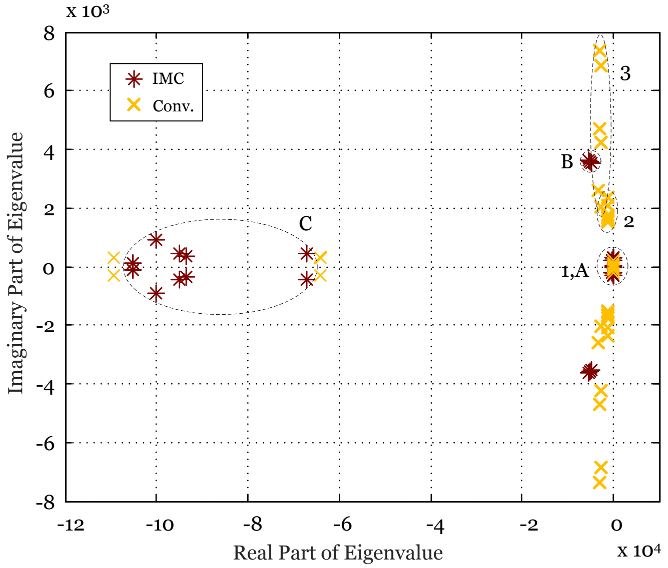

Fig. 5. IMC vs. conventional method: Locus of eigenvalues of the study microgrid grouped into clusters (Fig. 6 shows a close-up of the clusters 1—3 and A–B for $-6000 \leq \Re(\lambda) \leq 1000$).

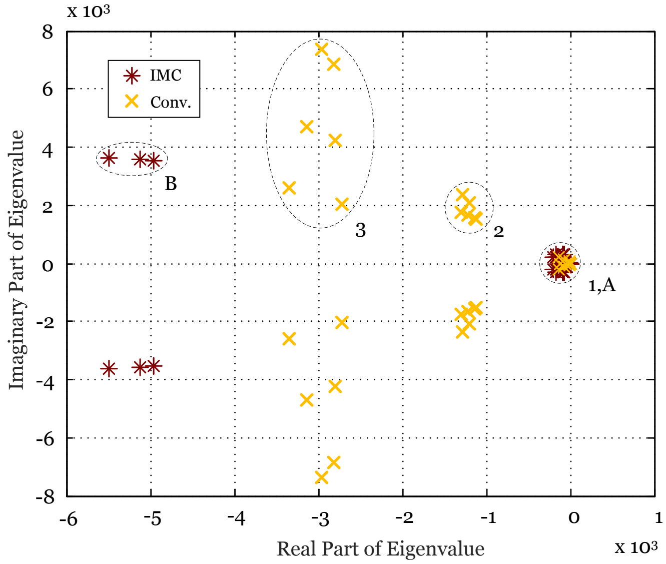

Fig. 6. IMC vs. conventional method: Locus of eigenvalues of the study microgrid grouped into clusters (close-up of Fig. 5).

TABLE II
SENSITIVITY OF CRITICAL IMC LOW-FREQUENCY DOMINANT MODES

Sensitivity of λ_{1-2}		**Sensitivity of λ_{1-3}**	
State	Participation	State	Participation
P_1	0.313	P_1	0.236
Q_1	0.109	Q_1	0.091
P_2	0.375	P_2	0.148
Q_2	0.106	P_3	0.384
P_3	0.066	Q_3	0.116

has eigenvalue clusters A, B, and C with IMC controllers, and eigenvalue clusters 1, 2, and 3 with PI controllers. Similar to the conventional PI-based approach, the IMC eigenvalues form a low-frequency cluster near the origin (cluster A in Figs. 5 and 6). The damping ratio ζ is defined as $\zeta = -\cos(\angle\lambda)$, where $\angle\lambda$ is the angle of the complex eigenvalue; hence, a small angle $\angle\lambda$ indicates a high damping ratio. As can be seen in Fig. 6, eigenvalues in clusters B and C of IMC have significantly improved damping ratios compared with clusters 2 and 3 of the conventional method. Cluster A, on the other hand, has more low-frequency eigenvalues than cluster 1 and is therefore studied in Figs. 7 and 8.

The participation factor relating the kth state variable to the ith eigenvalue, in a system with n eigenvalues, is defined as

$$p_{ki} = \frac{\lambda_i}{a_{kk}} = \frac{|v_{ki}||w_{ki}|}{\sum_{k=1}^{n} |v_{ki}||w_{ki}|}, \tag{29}$$

where λ_i is the ith eigenvalue, a_{kk} is the kth diagonal element of the system matrix, and w_{ki} and v_{ki} are the kth elements of the left and right eigenvectors associated with λ_i [30]. The participation factors of the most critical modes λ_{1-2} and λ_{1-3}, where the subscripts indicate the inverters with the highest participation factors, are listed in Table II. The participation factors show that, similar to the conventional approach studied in [11], low-frequency modes in cluster A are highly sensitive to the state variables of the power controller. Cluster B contains high-frequency modes sensitive to power controller state variables and output voltage Δv_{odq}, where the latter is a state variable of the filter and indirectly influences the state variables of the voltage controller, see (2). High-frequency modes in cluster C are sensitive to state variables of the filter and indirectly affect the state variables of the current controller, see (1).

B. Eigenvalue Sensitivity to Real Power Droop Gain

This subsection studies the sensitivity of the eigenvalues to the real power droop gain m_p to evaluate and compare the robustness and stability of both methods. The real power droop gain is varied between $1.57 \times 10^{-5} \leq m_p \leq 3.14 \times 10^{-4}$ as suggested in [11]. Fig. 7 shows the corresponding locus of low-frequency modes. The two critical eigenvalues of the sensitivity analysis listed in Table II are marked.

While the eigenvalues of the conventional control method deeply enter the right half plane and become unstable, IMC eigenvalues remain in the left half plane and retain stability. Fig. 7 confirms that the IMC approach has superior stability performance compared with the conventional approach.

C. Eigenvalue Sensitivity to Reactive Power Droop Gain

In this subsection, the sensitivity of eigenvalues to the reactive power droop gain n_q is studied. Fig. 8 shows the locus the of eigenvalues near the origin subsequent to a change in reactive power droop gain for $3.17 \times 10^{-4} \leq n_q \leq 7 \times 10^{-3}$ [11]. For IMC, eigenvalues located farther away from the real axis exhibit slightly larger imaginary parts compared with those of the conventional method. On the other hand, IMC eigenvalues located near the origin show slightly reduced real and imaginary parts compared with those of the conventional method as shown in Fig. 8. The eigenvalues of

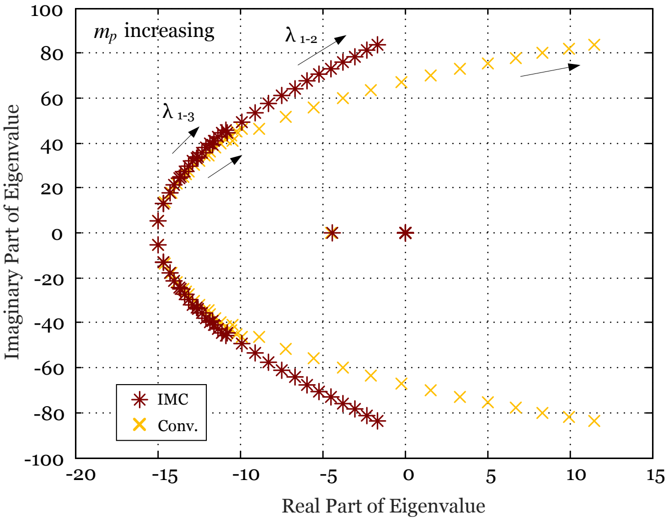

Fig. 7. IMC vs. conventional method: Locus of low-frequency modes as a function of real power droop gain (for $1.57 \times 10^{-5} \leq m_p \leq 3.14 \times 10^{-4}$).

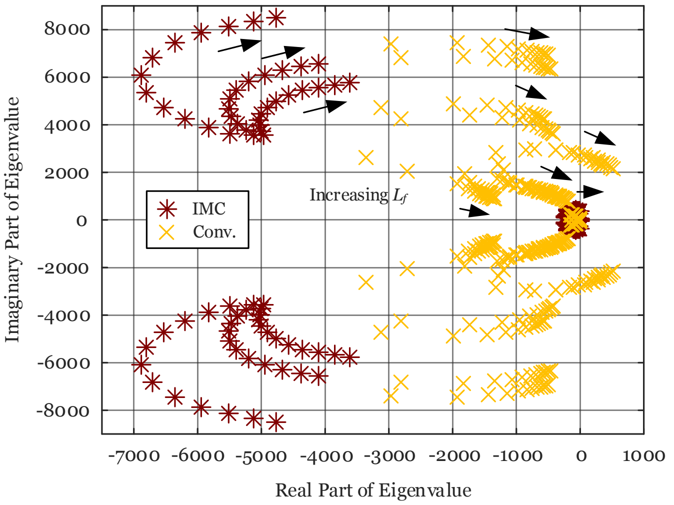

Fig. 9. IMC vs. conventional method: Locus of low-frequency modes as a function of filter inductance (for 1 pu $\leq L_f \leq$ 6.5 pu).

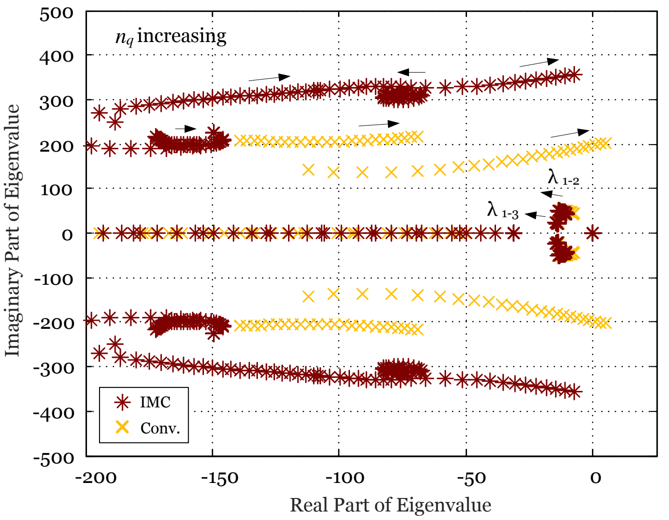

Fig. 8. IMC vs. conventional method: Locus of low-frequency modes as a function of reactive power droop gain (for $3.17 \times 10^{-4} \leq n_q \leq 7 \times 10^{-3}$).

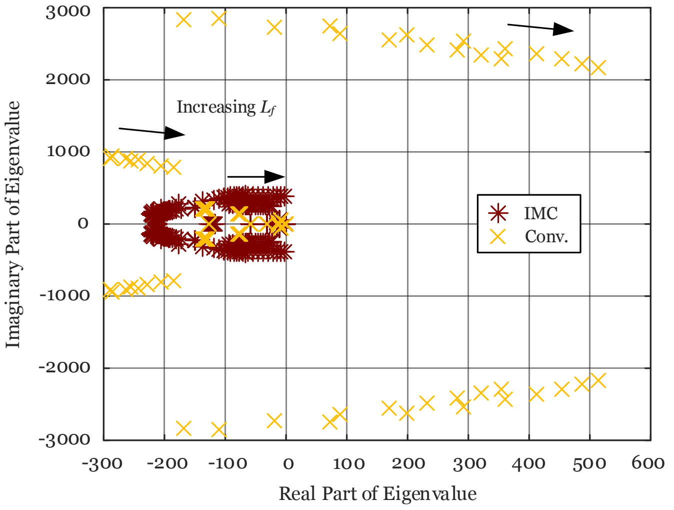

Fig. 10. IMC vs. conventional method (close-up): Locus of low-frequency modes as a function of filter inductance (for 1pu $\leq L_f \leq$ 6.5pu).

the conventional method become unstable by entering the right half plane for $3.17 \times 10^{-4} \leq n_q \leq 7 \times 10^{-3}$ while IMC eigenvalues remain in the left half plane and retain stability.

D. Eigenvalue Sensitivity to Filter Inductance L_f

In this subsection, the sensitivity of eigenvalues to the filter inductance L_f is studied for both methods. Fig. 9 shows the locus of the eigenvalues near the origin subsequent to a change in L_f in the range of 1 pu $\leq L_f \leq$ 6.5 pu. Sensitive eigenvalues of both methods travel toward the right half plane as L_f increases. Cluster B eigenvalues of IMC do not pose a stability threat as they remain far away from the right half plan. On the other hand, eigenvalues in cluster 2 and 3 of the conventional method quickly approach the right half plane and some become unstable.

Fig. 10 shows a close-up of the critical region around the origin of Fig. 9. As L_f increases, cluster A eigenvalues of the IMC method also approach the right half plane. As can be seen, the eigenvalues of the conventional method deeply enter the right half plane; however, eigenvalues of the IMC method retain stability for $L_f = 6.5$ pu. While these inductance values are rather large, they represent the stability limit of IMC (the conventional method becomes unstable for $L_f = 1.5$ pu). Hence, the IMC method is significantly more robust against parameter variations and uncertainties than the conventional method.

V. SIMULATION RESULTS

This section discusses simulation case studies to evaluate the performance of the IMC- and the PI-based approaches. The study microgrid shown in Figs. 2 and 4 is modeled in PSCAD/EMTDC environment. For the simulation case studies, the loads shown in Fig. 4 are excluded. Instead, for comparison with the results of [11], a large step change (from no load to 27 kW) is applied at bus 1 to specifically capture the high-frequency modes dominated by the voltage and current controllers (small R and large RL load step changes merely capture the low-frequency modes dominated by the power

This article has been accepted for publication in a future issue of this journal, but has not been fully edited. Content may change prior to final publication. Citation information: DOI 10.1109/TSG.2017.2688481, IEEE Transactions on Smart Grid

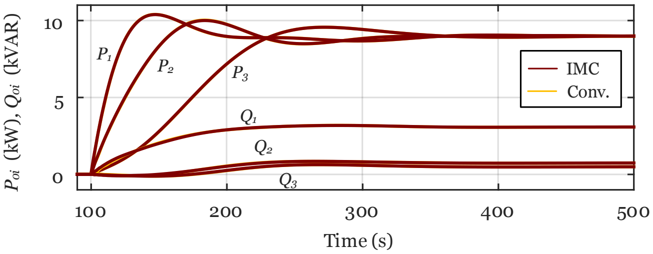

Fig. 11. IMC vs. conventional method: Real and reactive output power responses of DG units ($i = 1, 2, 3$) subsequent to a 27 kW step change in load power at bus 1.

controller, which are not the focus of this study). Furthermore, the results of the sensitivity analysis in Subsection IV-D are validated by changing the value of the filter inductance L_f.

A. Load Step Change

This subsection studies the response of the microgrid to a large load step change. Fig. 11 shows the response of real and reactive output power components of the three DG units caused by the step change in load at bus 1, comparing IMC and the conventional methods. The traces of both methods overlap, and only the IMC trace is visible. As anticipated, these methods have similar performance since they utilize the same power controller (while the current and voltage controllers are different). It can be seen that low-frequency modes of around 7 Hz in cluster A dominate the transient response in real and reactive power, which agrees with results of [11]. Because no load is connected to the microgrid before $t = 0.1$ s, both real and reactive output powers are zero. As a result of conventional droop control, eventually the 27 kW load is shared equally between the DG units while the reactive power is injected according to the feeder impedance between each DG unit and the load. The DG unit with the shortest electrical distance from the load change responds the fastest but also shows the largest overshoot.

Figs. 12(a) and (b) illustrate the d- and q-components of the filter current i_l responses of the three DG units, respectively, comparing IMC and conventional methods. Again, real power is shared equally since the d-components of the currents adjust to the same steady state value while q-components are according to reactive power sharing. Figs. 12(a) and (b) show that IMC has less overshoot and faster response than the conventional method, which agrees with [26], [27].

Fig. 13 shows transient responses of DG unit output voltages v_{odi} ($i = 1, 2, 3$) induced by the load step change. It can be seen that IMC significantly reduces the transient voltage undershoot. The conventional method causes voltage undershoots up to 20%. However, IMC has a maximum voltage undershoot of only about 1.7%. This behavior agrees with the results of a single DG unit case presented in [26], [27]. Reference [11] shows that the cluster 2 eigenvalues are responsible for the output voltage transients with frequencies around 350 Hz. IMC transients in the voltage show frequencies of around 1000 Hz and correspond to high-frequency modes in cluster B. Cluster B eigenvalues exhibit higher frequencies but have significantly improved damping ratios compared with cluster 2. This explains the drastic reduction of voltage undershoot with IMC.

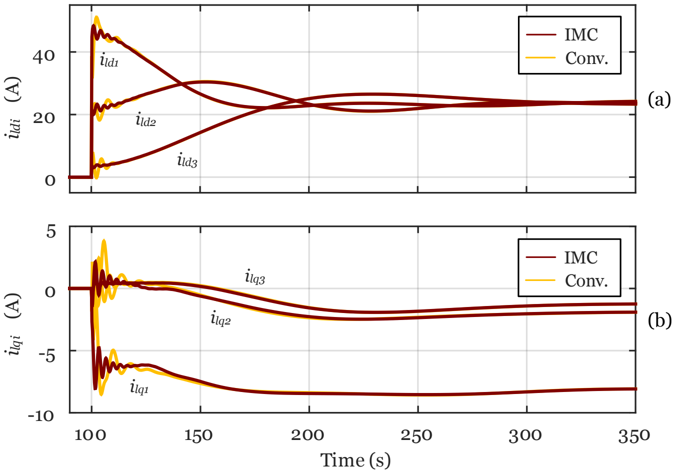

Fig. 12. IMC vs. conventional method: Filter current (d- and q-axis) responses of DG units ($i = 1, 2, 3$) subsequent to a 27 kW step change in load power at bus 1.

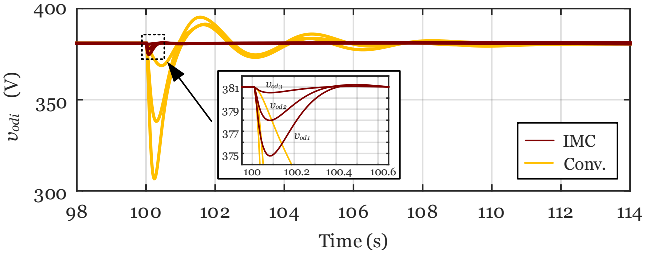

Fig. 13. IMC vs. conventional method: Output voltage (d-axis) responses of DG units ($i = 1, 2, 3$) subsequent to a 27 kW step change in load power at bus 1.

B. Sensitivity to Filter Inductance L_f

This subsection studies the sensitivity of the voltage and current controllers in the microgrid to parameter variations. Therefore, the same load step change as in Subsection V-A is applied while the value of the filter inductance is changed for both methods. Figs. 14(a) and (b) show the d- and q-components of the filter current i_l response of the three DG units, when the filter inductance L_f is increased to 1.5 pu for the conventional method and 6 pu for the IMC method. While the response of the conventional method show serious oscillations for an L_f increase of only 1.5 pu, the IMC method remains stable for increases up to $L_f = 6$ pu. Hence, the IMC voltage and current control is very robust against parameter variations of the filter. The results agree with those of the sensitivity analysis performed in Subsection IV-D, see Fig. 9 where the eigenvalues of the IMC method remain stable, i.e., in the left half plane for an L_f increase up to 6.5 pu while the eigenvalues of the conventional method have already entered the right half plane and lost stabiltiy.

It is important to point out that, due to poor damping ratios, waveforms of the PI-based approach also start oscillating earlier than those of IMC as the real and reactive power droop gain coefficients m_p and n_q increase (not presented in this paper). This agrees with the results of the small-signal analysis in Subsections IV-B and IV-C, which predict that the conventional method becomes unstable earlier than the IMC method as m_p and n_q increase (Figs. 7 and 8).

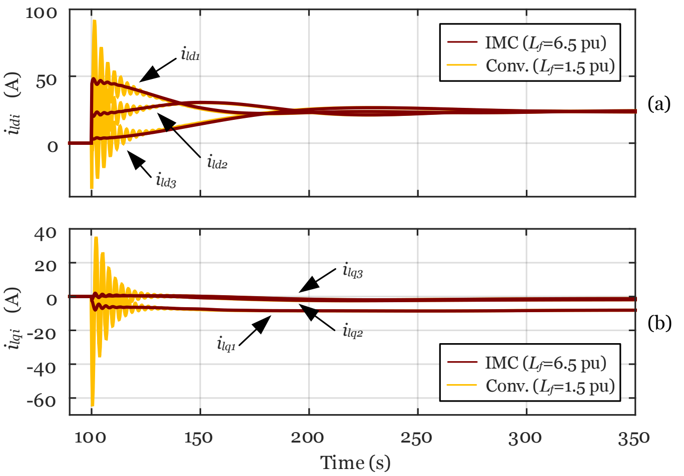

Fig. 14. IMC vs. conventional method - Parameter variation: Filter current (d- and q-axis) responses of DG units ($i = 1, 2, 3$) subsequent to a 27 kW step change in load power at bus 1 and filter inductance values of $L_f = 1.5pu$ (Conv.) and $L_f = 6pu$ (IMC).

VI. CONCLUSION

In this paper, a small-signal model of an inverter-based microgrid utilizing IMC-based controllers is derived. This model is used to perform eigenvalue and sensitivity analysis. Simulation case studies verify the results of this small-signal analysis. The results are compared with those of the same study microgrid utilizing conventional PI-based controllers. Sensitivity analysis, employing the calculation of participation factors, shows that low-frequency modes are highly sensitive to the parameters of the power sharing controller of the DG units for both methods. Varying these parameters (droop coefficients m_p and n_q), the eigenvalue plots reveal that, compared with the PI-based approach, the study microgrid with IMC controllers exhibits superior stability performance. Moreover, the microgrid with IMC controllers is significantly more robust against parameter uncertainties of the filter (L_f variation). Small-signal analysis shows that the reason for the drastically reduced voltage undershoot is the increased frequencies and damping ratios of sensitive eigenvalues.

REFERENCES

[1] D. Olivares, A. Mehrizi-Sani, A. Etemadi, C. Canizares, R. Iravani, M. Kazerani, A. Hajimiragha, O. Gomis-Bellmunt, M. Saeedifard, R. Palma-Behnke, G. Jimenez-Estevez, and N. Hatziargyriou, "Trends in microgrid control," *IEEE Trans. Smart Grid*, vol. 5, no. 4, pp. 1905–1919, Jul. 2014.

[2] M. Yazdanian and A. Mehrizi-Sani, "Distributed control techniques in microgrids," *IEEE Trans. Smart Grid*, vol. 5, no. 6, pp. 2901–2909, Nov. 2014.

[3] P. Tian, X. Xiao, K. Wang, and R. Ding, "A hierarchical energy management system based on hierarchical optimization for microgrid community economic operation," *IEEE Trans. Smart Grid*, vol. 7, no. 5, pp. 2230–2241, Sep. 2016.

[4] J. M. Carrasco, L. G. Franquelo, J. T. Bialasiewicz, E. Galvan, R. C. P. Guisado, M. A. M. Prats, J. I. Leon, and N. Moreno-Alfonso, "Power-electronic systems for the grid integration of renewable energy sources: A survey," *IEEE Trans. Ind. Electron.*, vol. 53, no. 4, pp. 1002–1016, Jun. 2006.

[5] P. Malysz, S. Sirouspour, and A. Emadi, "An optimal energy storage control strategy for grid-connected microgrids," *IEEE Trans. Smart Grid*, vol. 5, no. 4, pp. 1785–1796, Jul. 2014.

[6] M. Savaghebi, A. Jalilian, J. C. Vasquez, and J. M. Guerrero, "Secondary control scheme for voltage unbalance compensation in an islanded droop-controlled microgrid," *IEEE Trans. Smart Grid*, vol. 3, no. 2, pp. 797–807, Jun. 2012.

[7] R. H. Lasseter, "Microgrids," in *IEEE Power Eng. Soc. Winter Meeting*, Dec. 2002, pp. 305–308.

[8] F. Katiraei, R. Iravani, N. Hatziargyriou, and A. Dimeas, "Microgrids management," *IEEE Power Energy Mag.*, vol. 6, no. 3, pp. 54–65, May 2008.

[9] A. L. Dimeas and N. D. Hatziargyriou, "Operation of a multiagent system for microgrid control," *IEEE Trans. Power Syst.*, vol. 20, no. 3, pp. 1447–1455, Aug. 2005.

[10] F. Katiraei and M. R. Iravani, "Power management strategies for a microgrid with multiple distributed generation units," *IEEE Trans. Power Syst.*, vol. 21, no. 4, pp. 1821–1831, Nov. 2006.

[11] N. Pogaku, M. Prodanovic, and T. C. Green, "Modeling, analysis and testing of autonomous operation of an inverter-based microgrid," *IEEE Trans. Power Electron.*, vol. 22, no. 2, pp. 613–625, Mar. 2007.

[12] A. Bidram and A. Davoudi, "Hierarchical structure of microgrids control system," *IEEE Trans. Smart Grid*, vol. 3, no. 4, pp. 1963–1976, Dec. 2012.

[13] J. A. P. Lopes, C. L. Moreira, and A. G. Madureira, "Defining control strategies for microgrids islanded operation," *IEEE Trans. Power Syst.*, vol. 21, no. 2, pp. 916–924, May 2006.

[14] R. Majumder, B. Chaudhuri, A. Ghosh, R. Majumder, G. Ledwich, and F. Zare, "Improvement of stability and load sharing in an autonomous microgrid using supplementary droop control loop," *IEEE Trans. Power Syst.*, vol. 25, no. 2, pp. 796–808, May 2010.

[15] Y. Li, D. M. Vilathgamuwa, and P. C. Loh, "Design, analysis, and real-time testing of a controller for multibus microgrid system," *IEEE Trans. Power Electron.*, vol. 19, no. 5, pp. 1195–1204, Sep. 2004.

[16] C. K. Sao and P. W. Lehn, "Control and power management of converter fed microgrids," *IEEE Trans. Power Syst.*, vol. 23, no. 3, pp. 1088–1098, Aug. 2008.

[17] B. Kroposki, C. Pink, R. DeBlasio, H. Thomas, M. Simes, and P. K. Sen, "Benefits of power electronic interfaces for distributed energy systems," *IEEE Trans. Energy Convers.*, vol. 25, no. 3, pp. 901–908, Sep. 2010.

[18] M. Kazmierkowski and L. Malesani, "Current control techniques for three-phase voltage-source PWM converters: a survey," *IEEE Trans. Ind. Electron.*, vol. 45, no. 5, pp. 691–703, Oct. 1998.

[19] B. Bahrani, "Advanced control strategies for voltage source converters in microgrids and traction networks," Ph.D. dissertation, School of Engineering, Swiss Federal Institute of Technology (EPFL), 2012.

[20] C. Schauder and H. Mehta, "Vector analysis and control of advanced static VAr compensators," *IEE Proc. Gener. Transm. Distrib.*, vol. 140, no. 4, pp. 299–306, Jul. 1993.

[21] P. G. Barbosa, L. G. B. Rolim, E. H. Watanabe, and R. Hanitsch, "Control strategy for grid-connected DC-AC converters with load power factor correction," *IEE Proc. Gener. Transm. Distrib.*, vol. 145, no. 5, pp. 487–491, Sep. 1998.

[22] A. Yazdani and R. Iravani, "A unified dynamic model and control for the voltage-sourced converter under unbalanced grid conditions," *IEEE Trans. Power Del.*, vol. 21, no. 3, pp. 1620–1629, Jul. 2006.

[23] B. Bahrani, S. Kenzelmann, and A. Rufer, "Multivariable-PI-based *dq* current control of voltage source converters with superior axis decoupling capability," *IEEE Trans. Ind. Electron.*, vol. 58, no. 7, pp. 3016–3026, Jul. 2011.

[24] A. Mehrizi-Sani and R. Iravani, "Online set point modulation to enhance microgrid dynamic response: Theoretical foundation," *IEEE Trans. Power Syst.*, vol. 27, no. 4, pp. 2167–2174, Nov. 2012.

[25] ——, "Online set point adjustment for trajectory shaping in microgrid applications," *IEEE Trans. Power Syst.*, vol. 27, no. 1, pp. 216–223, Feb. 2012.

[26] M. Yazdanian and A. Mehrizi-Sani, "Internal model–based current control of the RL filter-based voltage-sourced converter," *IEEE Trans. Energy Convers.*, vol. 29, no. 4, pp. 873–881, Dec. 2014.

[27] ——, "Case studies on cascade voltage control of islanded microgrids based on the internal model control," in *9th IFAC Symp. Control of Power and Energy Syst. (CPES)*, New Delhi, India, Dec. 2015.

[28] F. Katiraei and M. R. Iravani, "Power management strategies for a microgrid with multiple distributed generation units," *IEEE Trans. Power Syst.*, vol. 21, no. 4, pp. 1821–1831, Nov. 2006.

[29] R. Majumder, B. Chaudhuri, A. Ghosh, R. Majumder, G. Ledwich, and F. Zare, "Improvement of stability and load sharing in an autonomous microgrid using supplementary droop control loop," *IEEE Trans. Power Syst.*, vol. 25, no. 2, pp. 796–808, May 2010.

[30] S. S. Damodhar and S. Krishna, "Comparison of participation factor method and selective eigenvalue computation for voltage stability analysis," in *8th Mediterranean Conf. Power Gen. Transm. Distrib. Energy Convers. (MEDPOWER)*, Oct. 2012.

Stefan Leitner (S'16) received the B.Sc. degree and the Dipl.-Ing. degree in electrical engineering from Graz University of Technology, Graz, Austria, in 2014 and 2016, respectively. He currently pursues the Ph.D. degree in electrical engineering at the Electric Drives and Machines Institute at Graz University of Technology, Graz, Austria.

He spent an academic year at the University of Tennessee, Knoxville, USA, in 2014–15, via the International Student Exchange Program (ISEP). He was a visiting scholar at Washington State University, Pullman, WA, USA, and a recipient of the Marshall Plan Scholarship in 2016. His research interests include electric drives, power electronics, and microgrids. He is a member of the Christian Doppler Laboratory - Brushless Drives for Pump and Fan Applications.

Mehrdad Yazdanian (S'10–GS'12) received the B.Sc. and M.Sc. degrees in electrical engineering from Isfahan University of Technology, Isfahan, Iran, in 2009 and 2012, respectively. He recieved his PhD degree in Electrical Engineering from Washington State University, Pullman, WA, USA.

He was a visiting scholar at Graz University of Technolgy, Graz, Austria, and a recipient of the Marshall Plan Scholarship in 2015. His research is focused on power system applications of power electronics, distributed control of microgrid, and application of filtering and estimation methods for power system monitoring. He is a member of the Energy Systems Innovation Center at Washington State University.

Ali Mehrizi-Sani (S'05–GS'08–M'12–SM'15) received the B.Sc. degrees in electrical engineering and petroleum engineering from Sharif University of Technology, Tehran, Iran, both in 2005. He received the M.Sc. degree from the University of Manitoba, Winnipeg, MB, Canada, and the Ph.D. degree from the University of Toronto, Toronto, ON, Canada, both in electrical engineering, in 2007 and 2011.

He is currently an Assistant Professor at Washington State University, Pullman, WA, USA. He was a Visiting Professor at Graz University of Technology, Graz, Austria, in Nov. 2014, Jan. 2016, and Nov. 2016. His areas of interest include power system applications of power electronics and integration of renewable energy resources.

Dr. Mehrizi-Sani is an editor of IEEE TRANSACTIONS ON POWER SYSTEMS, IEEE TRANSACTIONS ON POWER DELIVERY, and IEEE TRANSACTIONS ON ENERGY CONVERSION. He is also an editor of WILEY INTERNATIONAL TRANSACTIONS ON ELECTRICAL ENERGY SYSTEMS (ETEP). He is the Chair of IEEE TASK FORCE ON DYNAMIC SYSTEM EQUIVALENTS and the Secretary of the CIGRE Working Group C4.34 on Application of PMUs for Monitoring Power System Dynamic Performance. He was a recipient of the WSU VCEA Reid Miller Excellence in Teaching Award in 2016, the NSERC Postdoctoral Fellowship in 2011, and the Dennis Woodford prize for his M.Sc. thesis in 2007. He was a Connaught Scholar at the University of Toronto.

Annette Muetze (S'03–M'04–SM'09–F'16) received the Dipl.-Ing. degree in electrical engineering from Darmstadt University of Technology, Darmstadt, Germany, in 1999, the Diploma degree in general engineering from the École Centrale de Lyon, Écully, France, in 1999, and the Dr.-Ing. degree in electrical engineering from Darmstadt University of Technology in 2004.

She is currently a Professor with Graz University of Technology, Graz, Austria, where she heads the Electric Drives and Machines Institute. Prior to joining Graz University of Technology, she was an Assistant Professor with the Department of Electrical and Computer Engineering, University of Wisconsin, Madison, WI, USA, and an Associate Professor with the School of Engineering, University of Warwick, Coventry, UK. She is an editor of the IEEE TRANSACTIONS ON POWER ELECTRONICS and an editor of the IEEE TRANSACTIONS ON ENERGY CONVERSION. In 2004, she received the NSF CAREER award.